

# Microfluidic Synthesis of Multimode Au@CoFeB-Rg3 Nanomedicines and Their Cytotoxicity and Anti-Tumor Effects

Weiwei Zhang,<sup>▽</sup> Xiaoxiong Zhao,<sup>▽</sup> Yuan Yuan,<sup>▽</sup> Fenglin Miao, Wengang Li, Shaoxia Ji, Xing Huang, Xinhua Chen, Tianan Jiang, David A. Weitz, and Yujun Song\*

Cite This: <https://dx.doi.org/10.1021/acs.chemmater.0c00797>

Read Online

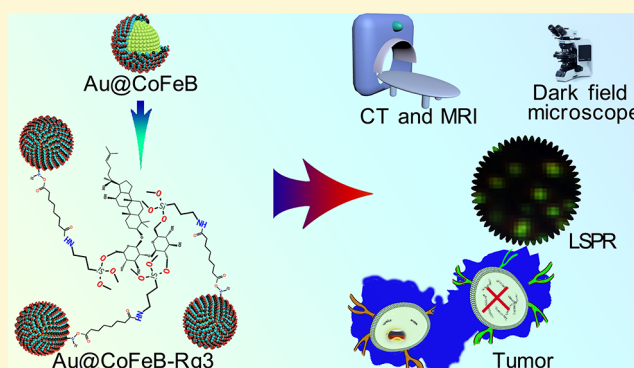
ACCESS |

Metrics & More

Article Recommendations

Supporting Information

**ABSTRACT:** Nanomedicines (i.e., Au@CoFeB-Rg3) were developed by conjugating multimode nanohybrids with active ingredients of natural herbs using Au@CoFeB nanoparticles as one model of multimode nanohybrids and the ginsenoside Rg3 as one model of active ingredients of natural herbs. Au@CoFeB nanoparticles were first synthesized using a temperature-programmed microfluidics process. Then, the surface of Au@CoFeB nanoparticles was modified via an amino-silane coupling agent of (3-aminopropyl) trimethoxysilane (APTMS) and then activated by the bifunctional amine-active cross-linker. They were thereafter conjugated to ginsenosides preactivated by APTMS by cross-linking the surface-activated nanohybrids, forming Au@CoFeB-Rg3 nanomedicines. Their multimode imaging functions were evaluated with the characterization of their magnetic and optical properties and the response to X-ray radiation. They can be optically detected via dark-field microscopy and can be imaged through X-ray computed tomography. They can also be used as magnetic resonance imaging contrast agents with excellent T2-weighted spin-echo imaging effects. Au@CoFeB-Rg3 nanomedicines exhibited distinct cytotoxicity and inhibitory effects on the proliferation of human hepatocellular carcinoma cells (HepG2/C3) and human chronic myeloid leukemia cells (K562) but were less toxic to 3T3 cells than other cells at concentrations more than 200  $\mu\text{g}/\text{mL}$ . However, Au@CoFeB nanoparticles showed markedly lower cytotoxicity and inhibitory effects on the proliferation of these cell lines, particularly at concentrations <100  $\mu\text{g}/\text{mL}$ , than Au@CoFeB-Rg3 nanomedicines. Clearly, there is a distinct synergistic effect between nanohybrids and Rg3. Additionally, Au@CoFeB nanohybrids showed almost no toxicity to Jurkat-CT cells at low concentrations (47  $\mu\text{g}/\text{mL}$ ), indicating that they may be used as multimode nanoprobe at a suitable concentration. These findings provide an efficient alternative for the synthesis of multifunctional antitumor nanomedicines based on multimode nanohybrids and active ingredients of natural resources.



## INTRODUCTION

Nanomedicines (NMs) are applicable to monitoring and control, diagnosis and therapy, and tissue repair of biological systems at the molecular level, owing to their controllable size, large surface area-to-mass ratios, and unique physicochemical properties.<sup>1</sup> In recent years, the primary approaches to the synthesis of NMs have been focused on the following aspects: (1) diagnosis for obtaining coherent results by improving the sensitivity and integration of analytical methods,<sup>2–11</sup> (2) drug delivery for carrying the bioactive agents,<sup>12–16</sup> (3) tissue engineering and implants for overcoming limitations associated with vascular grafts,<sup>17–20</sup> and (4) bioavailability improvement<sup>21–23</sup> and medical devices.<sup>24</sup> In addition, a broad range of nanomaterials have been used for the translation to NMs, which include nanosuspensions,<sup>25</sup> polymeric nanoparticles (NPs),<sup>26–28</sup> iron oxide NPs,<sup>29</sup> metallic NPs,<sup>30,31</sup> nanopores,<sup>32</sup> dendrimers,<sup>33</sup> liposomes,<sup>34</sup> etc. Therefore, NMs have improved and extended the pharmacokinetic, solubility and

stability properties of a series of drug molecules that have been widely used in various biomedical applications, including particular drug delivery, therapy, imaging, and diagnostics.<sup>1,35</sup> However, the use of NMs continues to be characterized by numerous unclear effects on human health and various biological barriers to be overcome, which include stability, surface modification and functionalization, multimode functions, efficient drug delivery, a balance between the efficacy and side effects, etc.<sup>1,36</sup>

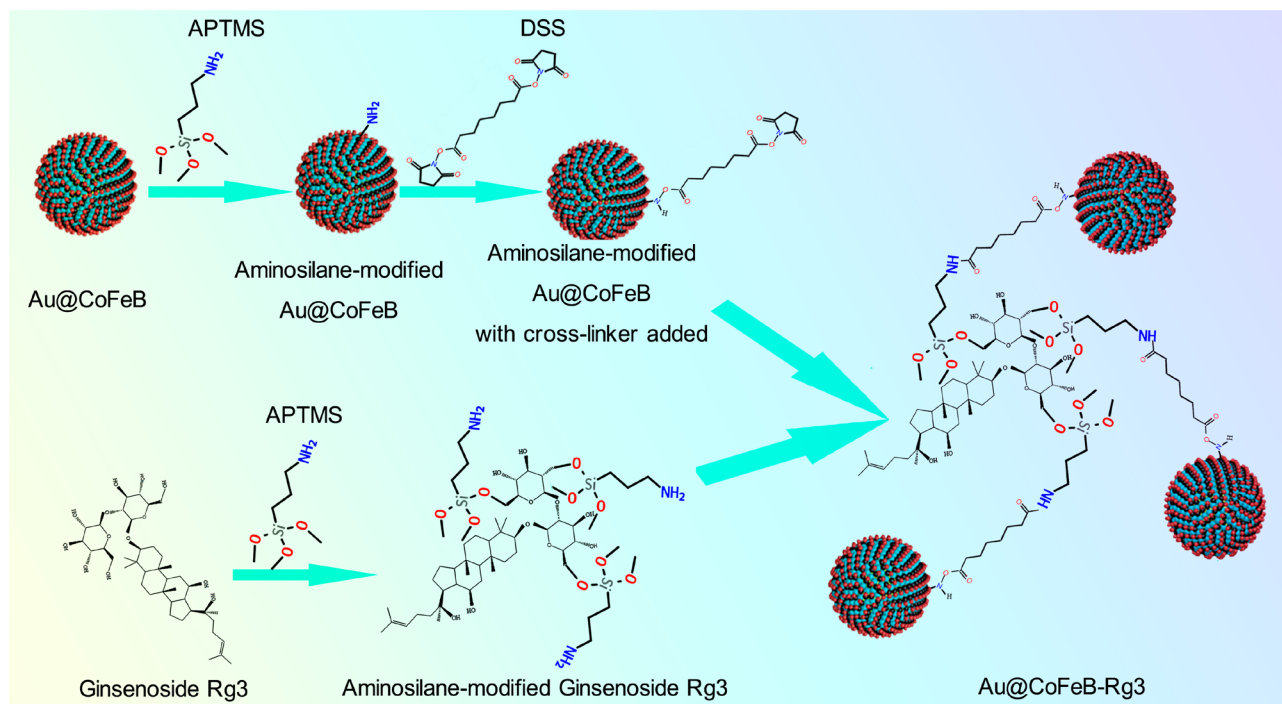
Nanohybrids (NHs) consisting of noble metal and magnetic components are promising for applications in a broad range of

Received: February 26, 2020

Revised: May 12, 2020

Published: May 12, 2020

Scheme 1. Chemical Reaction Process of the Synthesis of the Au@CoFeB-Rg3 NMs



areas including energy conversion,<sup>37,38</sup> medical imaging,<sup>39,40</sup> and disease detection,<sup>41–43</sup> owing to their unique physicochemical properties, high stability, and multimode properties (i.e., magnetic and electromagnetic sensitivity).<sup>44</sup> Moreover, proper modification of the surface of these NPs and/or conjugation with certain medicines or organic components leads to a wide therapeutic window and clinical application with no or markedly reduced side effects on healthy cells and/or tissues. These alterations have rendered certain NHs useful as effective chemotherapeutic drugs for numerous diseases owing to their appealing features for diagnosis, imaging, drug delivery, therapy, and even the development of synthetic vaccines.<sup>45</sup> Thus, the controlled synthesis and functionalization of multimode NHs have continuously received great attention for expanding their interdisciplinary applications to fundamental studies and clinical application (e.g., ultrasensitive bioprobes,<sup>46,47</sup> high efficient NMs and nanoenzymes,<sup>48</sup> ultrasensitive biomedical molecule imaging and diagnosis of some diseases<sup>49–52</sup>). These biomedical applications have been primarily driven by the intrinsic physicochemical properties and surface modification of NMs. These can be flexibly tailored by altering their size, construction components, surface/interface topography, and functionalization.<sup>48,53,54</sup> For these goals, lots of advanced synthesis technologies have been developed.<sup>55–58</sup> Among them, the well-established microfluidic process has been recognized as an effective methodology rather than the conventional batch processes owing to the precise control of reaction conditions during nanomedicine synthesis.<sup>54,59–63</sup> This approach affords narrow size distribution and good control over the shape and size of the core-shell NPs owing to the precise spatiotemporal resolution control of the kinetic parameters of each stage during the NP formation.<sup>54,62,64,65</sup>

In this study, Au@CoFeB NHs were synthesized, and their conjugation with ginsenoside Rg3 was conducted to form NMs (i.e., Au@CoFeB-Rg3) for future use in multimode diagnosis

and cancer therapy. In contrast to gemcitabine, fluorouracil, oxaliplatin, and nab-paclitaxel that fail to effectively inhibit tumor progression, the ginsenoside Rg3 has become increasingly popular in the treatment of cancer owing to its broad efficacy and low side toxicity, as well as its boosting effect on the immunity of patients.<sup>66</sup> Ginsenoside Rg3, a steroidal saponin with high pharmacologic activities, is an efficient anticancer therapeutic agent. It can promote TRAIL-induced apoptosis in several hepatocellular carcinoma cell lines, including HepG2, SK-Hep1, Huh-7, and Hep3B,<sup>67</sup> suggesting that Rg3 sensitization to TRAIL might be specific to cancer cells. Moreover, Rg3 exhibits excellent anticancer activities in *in vitro* cell experiments and animal experiments *in vivo*, and ginsenosides have been used to improve the immunity of people.<sup>66</sup> These activities include apoptosis, angiogenesis suppression, metastasis inhibition, chemotherapy efficacy enhancement, and survival prolongation.<sup>67–69</sup> The mechanism underlying the increase in chemotherapy efficacy improvement is postulated to be via its inhibitory effects on NF- $\kappa$ B and AP-1.<sup>70</sup> There are two stereoisomers in Rg3, namely, 20(S)-Rg3 and 20(R)-Rg3. The main difference between them lies in the spatial selectivity of the hydroxyl group of carbon atom no. 20 on the molecular structure. In this paper, 20(R)-Rg3, which has a good effect on liver cancer therapy, was used.

The tiny Au nanoparticles that have already been synthesized provide surface templates or substrates on which CoFeB layers can deposit and grow. The alloyed metalloid boron component that is a necessary dietary component for humans and animals can provide a supplement used in nanomedicine, possibly exhibiting a promising synergistic therapeutic effect since borax has been widely used in traditional Chinese drugs due to a heat-clearing and detoxifying effect that is also beneficial to the immunological system.<sup>71</sup> Amazingly, it has been experimentally demonstrated that Au@CoFeB NPs and Au@CoFeB-Rg3 NMs show

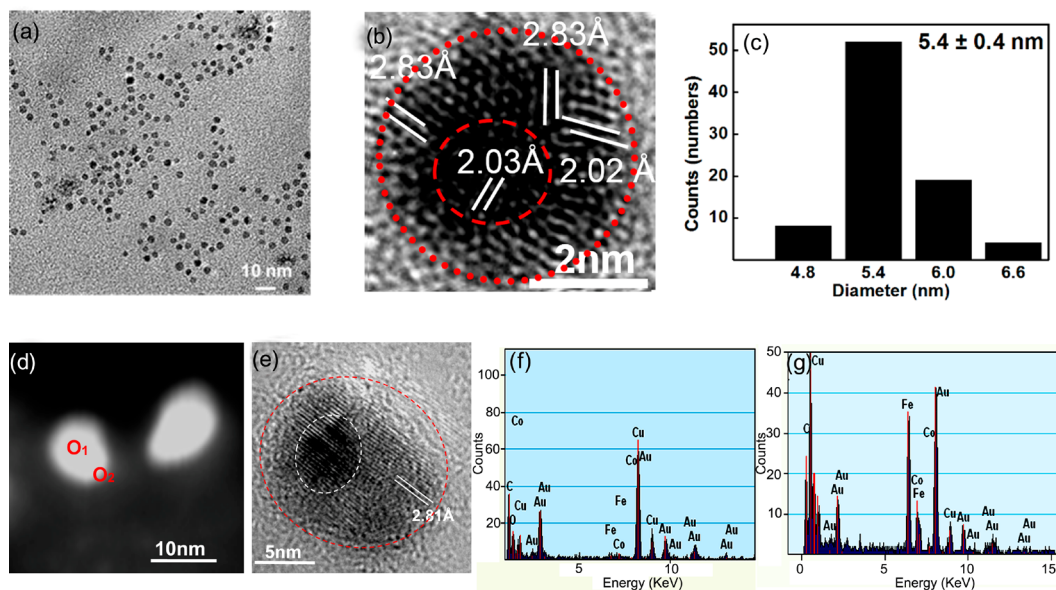


**Figure 1.** (a) Wide-view TEM image of the Au@CoFeB NPs. (b) HR-TEM image of one single NP showing the lattice fringe of 2.03 Å in the core and the lattice fringe of 2.02 and 2.83 Å in the shell. (c) The histogram of the size distribution of the Au@CoFeB NPs. (d) The high-angle annular dark field (HAADF) STEM image and (e) the corresponding HR-TEM image of one typical NP. (f) The EDS spectra of point 1 in the center of the single NP and (g) the EDS spectra of point 2 in the outer shell of the single NP to show distinctly increased Au content and decreased Co and Fe contents in the center of the single NP.

multimode imaging functions for medical diagnosis and exhibit a marked effect on the treatment of cancer cells. These NHs can be observed optically under a dark field microscope when used to tag biological molecules for the precise study of cell–medicine interaction. They can also be used in noninvasive magnetic resonance imaging (MRI) for future clinical applications. Particularly, the Au@CoFeB-Rg3 NMs enhance computed tomography (CT), which can improve the accuracy of clinical diagnosis/imaging. Furthermore, they exert distinct antitumor effects that are significantly toxic to K562-CT cells and Hep-G2/C3A cells, and distinctly inhibit the proliferation of these cancer cells.

## EXPERIMENTAL SECTION

The synthesis process of the Au@CoFeB-R3 NMs was elucidated in Scheme 1. Surface hydroxyl groups of Au@CoFeB NPs were modified to become amino groups using modifier 3-aminopropyl trimethoxysilane (APTMS). Subsequently, they were activated by a bifunctional amine-active cross-linker (i.e., disuccinimidyl suberate (DSS)). Finally, the preactivated ginsenoside Rg3 with APTMS was conjugated to the above surface modified NPs, forming the desired Au@CoFeB-Rg3 NMs. Please refer to the details in the Supporting Information.

## RESULTS AND DISCUSSION

**Morphology, Structure, and Composition of Synthesized NPs.** The wide-view transmission electron microscopy (TEM) image shown in Figure S1a in the Supporting Information reveals well-dispersed spherical CoFeB NPs. According to the statistics of more than 100 randomly selected NPs, these NPs have a narrow size distribution with an average size of  $2.4 \pm 0.6$  nm, as shown in the histogram of sizes (Figure S1b). The alloyed NPs are smaller than Co NPs due to the higher reaction temperature in the process of CoFeB NPs synthesis.<sup>72</sup> This is attributed to the shortening of the growth time of NPs by performing the synthesis of the CoFeB at a relatively faster flow rate (3 mL/min) compared with that of

the Co NPs (0.8 mL/min). The NPs are clearly highly crystalline as observed from the high resolution TEM (HR-TEM) images, as evidenced by one typical particle image inserted into Figure S1a. Furthermore, the lattice spacing of 2.02 Å measured from the high-resolution image can be indexed to the (110) plane of the body center cubic (bcc) CoFeB alloy. As detailed in Figure S1c, the X-ray powder diffraction (XRD) curve of the precursor CoFeB NPs indicates that the peak positions which are located at  $31.32^\circ$  and  $45.58^\circ$  can be indexed as the (100) and (110) planes (JCPDS: 44-1433). The (110) plane in the XRD curve is determined to be in good agreement with the HR-TEM image. In addition, the positions located at  $58.06^\circ$ ,  $66.33^\circ$ ,  $75.25^\circ$ , and  $84.17^\circ$  are found to correspond to the (111), (200), (210), and (211) planes of the bcc CoFeB phase (JCPDS: 44-1433), respectively.

According to the statistics of more than 100 randomly selected NHs, the synthesized Au@CoFeB NPs display a spherical shape (Figure 1a), with an average diameter of  $5.4 \pm 0.4$  nm (Figure 1c). The HR-TEM image (Figure 1b) clearly reveals the core–shell structure and good crystallization, with a lattice spacing of 2.03 Å in the core (corresponding to the face center cubic (fcc) Au (200)) and lattice spacings of 2.83 and 2.02 Å on the surface (corresponding to the (100) and (110) planes of bcc CoFeB, respectively). On the basis of the results of this study, it is clear that the (110) plane of the bcc CoFeB matches the (200) plane of the fcc Au. The composition distributions of the NPs were characterized by an energy dispersive X-ray spectrum (EDS) to further confirm the structures of the core–shell. Figure 1d–g show the high-angle annular dark field (HAADF) scanning TEM images and EDS spectra of the relative Co, Fe, and Au distributions in the center and edges of a representative NH. The EDS spectrum confirms that the central parts of the NHs are mainly composed of Au, as well as some Co and Fe, as indicated by the strong Au peaks and indistinct Co and Fe peaks (Figure



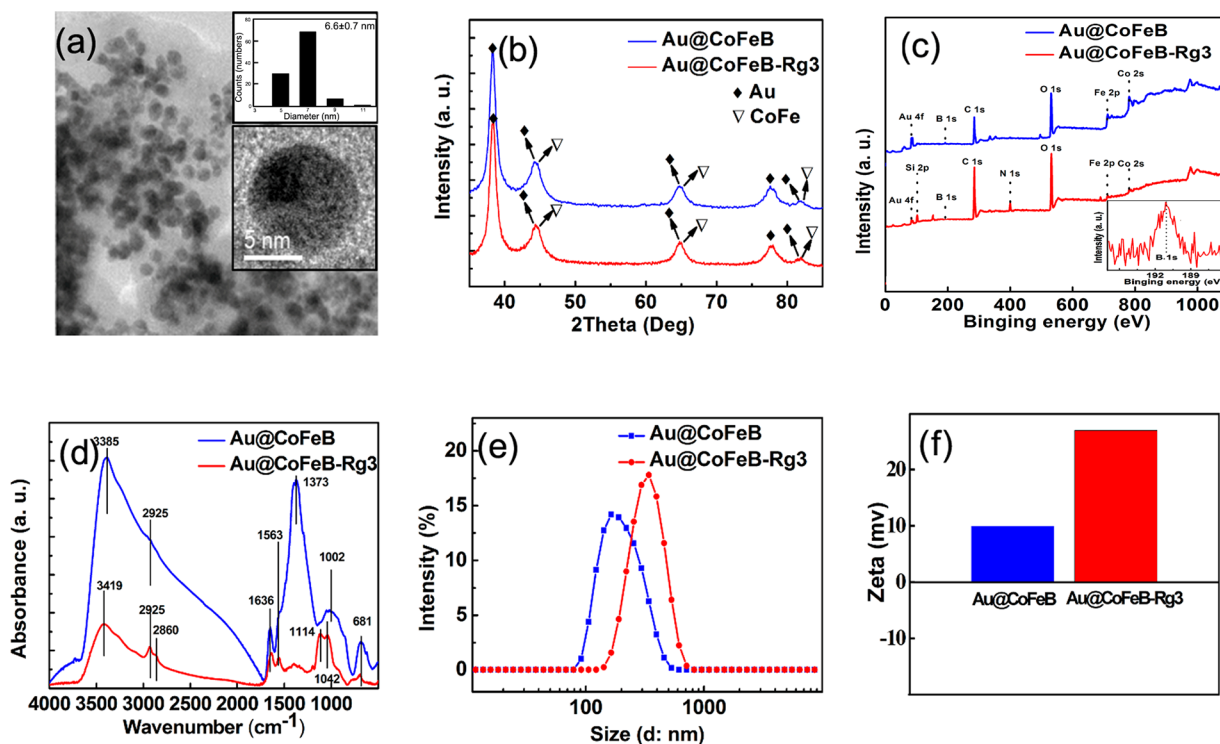


**Figure 2.** (a) Wide view TEM image of Au@CoFe(B)-Rg3 NMs (the inserted are the HR-TEM image of one single NM and the histogram of the size distribution). (b) X-ray diffraction, (c) full X-ray photoelectron spectroscopy (XPS) spectra (the inserted image is XPS of boron binding energy of the NMs), (d) Fourier transform infrared spectroscopy (FT-IR), (e) hydrodynamic radius, and (f) zeta potential results of the prepared Au@CoFe(B) (blue curve or column) and Au@CoFe(B)-Rg3 NMs (red curve or column).

1f). However, the intensity of the Au peak on the edges is reduced compared with that of the peaks in the central parts of the NPs, and the Co peak and the Fe peaks become the most intensive peaks (Figure 1g). This result suggests that the core of the sample is mainly composed of Au, while the shell is mainly composed of CoFeB. The Au/Co/Fe/B atom ratio is approximately 1/2.2/1.8/2.2, as confirmed by the inductively coupled plasma optical emission spectrometer (ICP-OES) data (detailed experimental process, see the [Supporting Information](#)). As shown in the XRD spectrum of the Au@CoFeB NPs in Figure S2a, the diffraction peaks corresponding to the CoFeB and Au phases are observed, confirming the formation of the Au@CoFeB NPs architecture in the microfluidic reductions. The peak position at  $44.83^\circ$  can then be indexed as the (110) plane of CoFeB, which matches the HR-TEM image shown in Figure 1b. In addition, the peak positions located at  $65.26^\circ$  and  $82.66^\circ$  can be indexed as the (200) and (211) planes of the bcc-CoFeB (JCPDS: 44-1433), respectively. The peak positions located at  $38.75^\circ$ ,  $44.88^\circ$ ,  $65.50^\circ$ ,  $78.08^\circ$ , and  $82.42^\circ$  are successfully indexed as the (111), (200), (220), (311), and (222) planes of the fcc-Au (JCPDS: 04-0784), consistent with the previous reports.<sup>73</sup> X-ray photoelectron spectroscopy (XPS) was performed to determine the elemental composition, as well as the chemical and electronic state. As shown in Figure S2b, the Au@CoFeB NPs consist of Au, B, C, O, Fe, and Co, matching the proposed reaction processes. The Au@CoFeB NPs were further analyzed through Fourier-transform infrared spectroscopy (FT-IR). The FT-IR spectrum of Au@CoFeB NPs was investigated in the range from  $500\text{ cm}^{-1}$  to  $4000\text{ cm}^{-1}$ . As detailed in Figure S2c, the peak at  $3385\text{ cm}^{-1}$  is assigned to the  $-\text{OH}$  group (surface  $-\text{OH}$  group of NPs). The peak at  $2925$

$\text{cm}^{-1}$  is ascribed to the  $\text{CH}_3/\text{CH}_2$  groups from the surface-coated surfactant,<sup>74</sup> while the peak at  $1636\text{ cm}^{-1}$  for the Au@CoFeB NPs represents the stretching vibration of  $\text{C}=\text{O}$  in the polyethylene chain of PVP. Compared with the diameter ( $5.4 \pm 0.4\text{ nm}$ ) shown in the TEM image (Figure 1c), the hydrodynamic radius of Au@CoFeB ( $\sim 164\text{ nm}$ ) NPs in Figure S2d is markedly higher. This is because the magnetism in the particles results in their accumulation into larger NPs in ethanol. Moreover, as shown in Figure S2e, Au@CoFeB NPs show positive electrical potential. This positive zeta potential with the hydrodynamic radius favors the endocytosis of NPs owing to the negative electrical potential exhibited by most cells.

The wide-viewed TEM image of Au@CoFeB-Rg3 NMs shown in Figure 2a reveals that these NMs can be well-dispersed. Even after the surface modification and conjugation with ginsenoside Rg3 that results in the lattice fringe being unclear, the core-shell nanostructure is still distinct and the NMs have a uniform size with a mean diameter of  $6.6 \pm 0.7\text{ nm}$  (inserted images in Figure 2a). As shown in Figure 2b, compared with the XRD pattern of the Au@CoFeB (blue curve), the peaks in the Au@CoFeB-Rg3 (red curve) become slightly sharper, revealing that the surface modification and conjugation processes improve the crystallinity. XPS characterization was performed after modification of the surfaces of Au@CoFeB NPs with (3-aminopropyl)trimethoxysilane (APTMS)-modified ginsenoside Rg3. As shown in Figure 2c, compared with the Au@CoFeB (blue curve), the Au@CoFeB-Rg3 NMs (red curve) consist of Au, Si, B, C, N, O, Fe, and Co, matching the proposed mechanisms of nanoparticle formation and conjugation reaction, detailed in the [Supporting Information](#). The Au, Fe, Co, and B are derived from the

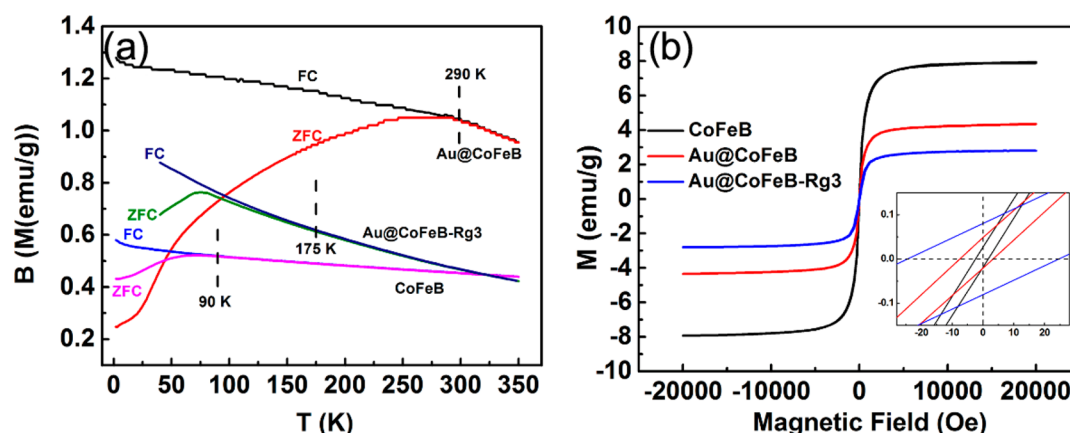


**Figure 3.** (a) ZFC/FC curves and (b) magnetic hysteresis loops of CoFeB NPs, Au@CoFeB NPs, and Au@CoFeB-Rg3 NMs.

Au@CoFeB NPs. N is derived from the surface modification agent (APTMS) and the linking agent (di(N-succinimidyl) suberate), while Si is apparently derived from the surface modification agent (APTMS). The NMs were further analyzed by FT-IR. Figure 2d shows the FT-IR spectra of Au@CoFeB NPs and Au@CoFeB-Rg3 NMs. As detailed in its FT-IR spectrum of Au@CoFeB-Rg3 NMs, following the conjugation with ginsenoside Rg3 to NPs modified by APTMS and DSS, the typical dual absorbance peaks for ginsenoside Rg3 (at 1077  $\text{cm}^{-1}$  and 1042  $\text{cm}^{-1}$ )<sup>74</sup> are 1042  $\text{cm}^{-1}$  and 1114  $\text{cm}^{-1}$ , respectively (Figure 2d, red curve). The combination of the XPS and FT-IR analysis confirms the proposed conjugating mechanism, and the Au@CoFeB-Rg3 NMs are successfully synthesized.

As shown in Figure 2e, after the surface modification and conjugation processes, the hydrodynamic radius of Au@CoFeB-Rg3 (~342 nm) NMs (red curve) is markedly increased by comparing with that of Au@CoFeB (~164 nm) NPs after the introduction of the ginsenoside Rg3 onto the NHs. Moreover, the coupling effect leads to a size increase of nanomedicines as observed from their TEM image (Figure 2a). Furthermore, as shown in Figure 2f, the positive electrical potential of Au@CoFeB-Rg3 (red column) is increased due to the introduction of  $-\text{NH}_2$  on the surface of NHs during the surface modification and coupling process. The positive zeta potential favors the endocytosis of NPs and NMs owing to the negative electrical potential exhibited by most cells.

**Optical and Magnetic Properties.** Figure S3 shows the UV-vis absorbance spectra of the CoFeB NPs (curve i), pure Au (curve ii), Au@CoFeB nanocolloids prepared through centrifugation (curve iii) and after magnet adsorption (curve iv), and Au@CoFeB-Rg3 NMs (curve v). There is no distinct absorption peak observed for the CoFeB NPs from 400 to 900 nm. However, there is a resonance position for Au@CoFeB NPs, and the peak positions exhibit a red shift, compared with that of the pure Au NPs. A slight blue shift is noticed for the sample prepared through centrifugation, compared with that of the sample prepared through adsorption. This is attributed to the mixing of the sample after centrifugation with Au and Au@CoFeB NPs, and the small number of elemental Au particles in the NPs in the solutions prepared through magnet adsorption. It has been previously reported that Au NPs with a size ranging 3 to 20 nm showed distinct localized surface plasmon resonance (LSPR) with absorbance positions at approximately 500–550 nm.<sup>75,76</sup> It was shown that the amplitudes and peak positions were obviously dependent on the sizes, shapes,

dielectrics, and orientation of the gold particles and their interspacing, as well as the environmental medium around the particles.<sup>77–80</sup> The environmental media included the substrate used to fix the gold particles, as well as the surrounding medium or shells (e.g., CoFeB in this study) attached to the Au particle surfaces. In this study, as shown in curve ii, the Au NPs display a distinct LSPR peak at 526 nm, which is consistent with previous reports.<sup>79,80</sup> The coated magnetic component CoFeB on the Au surfaces strongly affects surface plasmon resonance. It is found that the presence of the CoFeB shells endows the core-shell NPs with a strong red shift (~558 nm; curve iii). This shift is assigned to variations in the local dielectric environment of the gold and different refractive indexes between the Au and CoFeB according to the Mie theory for nanospheres.<sup>81,82</sup> This type of phenomenon has been observed in other core-shell NPs with Au cores.<sup>83</sup> In addition, after the surface modification and conjugation with ginsenoside Rg3, the LSPR peak can extend to ~563 nm (curve v) due to the further change of the local dielectric environment around the Au core.

The Au cores also endowed the Au@CoFeB NPs and Au@CoFeB-Rg3 NMs with unique magnetic properties compared with the pure CoFeB NPs (Figure 3a and b) by hybridization and interface interaction. Their magnetic properties are summarized in Table 1. The ZFC (zero-field cooling) and

**Table 1. Magnetic Properties of NPs<sup>a</sup>**

sample	Hc, Oe		$M_{0,t}$ and $M_{0,b}$ , emu/g		$M_s$ , emu/g	Tb, K
	left	right	$M_{0,t}$	$M_{0,b}$		
CoFeB	−2.6	1.7	0.024	−0.019	7.98	90
Au@CoFeB	−7.6	3.1	0.048	−0.021	4.36	290
Au@CoFeB-Rg3	−25.5	24.6	0.08	0.008	2.52	175

<sup>a</sup>Hc, coercivity;  $M_{0,t}$  and  $M_{0,b}$ , magnetism at the zero field in the top and bottom hysteresis;  $M_s$ , magnetic saturation; Tb, blocking temperature.

FC (field cooling) curves, measured under an applied field of 100 Oe (Figure 3a), suggest a superparamagnetic nature of the CoFeB, Au@CoFeB, and Au@CoFeB-Rg3 samples at room temperature. Furthermore, approximately estimated from the ZFC and FC curves in Figure 3a, the blocking temperature (Tb; temperature from the ferromagnetic to the paramagnetic transition) of the Au@CoFeB NPs is increased to 290 K compared to that of the pure CoFeB NPs (90 K). In

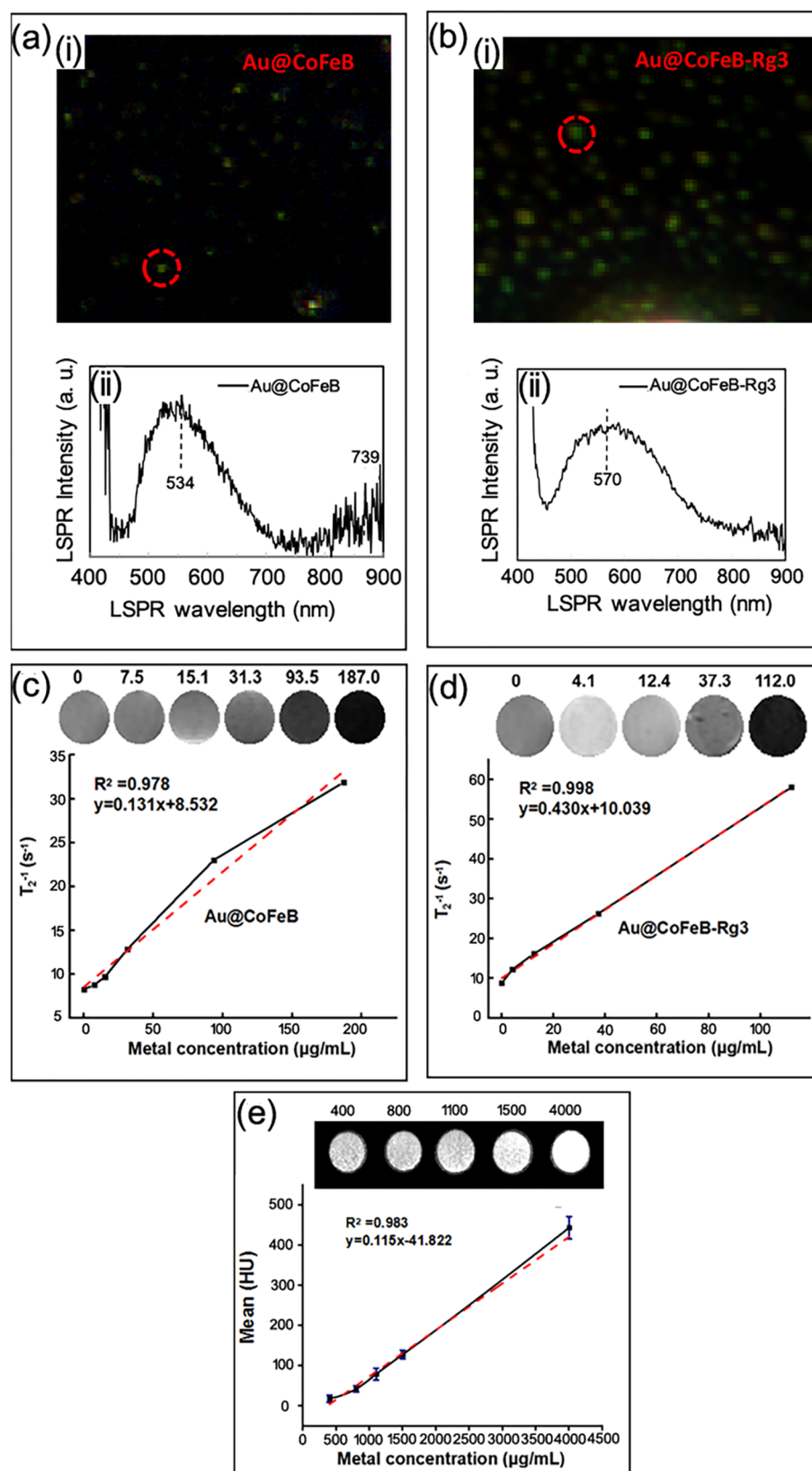


**Figure 4.** LSPR real color images of (a-i) Au@CoFeB NPs and (b-i) Au@CoFeB-Rg3 NMs and their LSPR spectra (a-ii, Au@CoFeB; b-ii, Au@CoFeB-Rg3) measured by dark-field microscopy and spectroscopy. MRI effects of Au@CoFeB and Au@CoFeB-Rg3 solutions. (c) The effective metal (Co and Fe) concentration-dependent  $T_2$  relaxation rates and MR images (top images) of Au@CoFeB NPs generated on a  $T_2$ -weighted spin-echo sequence with an echo time (TE) of 33 ms and a pulse repetition time (TR) of 2500 ms. (d) The effective metal (Co and Fe) concentration-dependent  $T_2$  relaxation rates and MR images (top images) of Au@CoFeB-Rg3 NPs generated on a  $T_2$ -weighted spin-echo sequence with a TE of 33 ms and a TR of 2500 ms and (e) CT signal intensity of Au@CoFeB-Rg3 NPs depending on the overall contrast agent concentration (500–4500  $\mu\text{g/mL}$ ; voltage, 80 kV; current, 499  $\mu\text{A}$ ; spot size, 50  $\mu\text{m}$ ).



accordance with the general expression of the  $T_b$  for magnetic NPs, an increase in  $T_b$  should be mainly the consequence of increased magnetic anisotropy, or possibly relatively increased volumes of the magnetic shells in the NPs<sup>84–86</sup> and the enhanced magnetic interactions among the particles after the drying step.<sup>53</sup> In this study, the increased  $T_b$  is mainly attributed to the enhanced magnetic surface anisotropy caused by the strong pinning effects of the CoFeB spins at the CoFeB/Au interface.<sup>87</sup> In general, magnetic anisotropy increases the coercivity of particles, whereas the magnetic dipole interaction among particles during measurements induces the opposite effect.<sup>86,88,89</sup> Therefore, the increased coercivity of the Au@CoFeB NPs is assigned to the enhanced magnetic anisotropy and the reduced interparticle dipole interactions. It is also not surprising that there is a lower magnetic saturation observed in the Au@CoFeB NPs (Ms: 4.36 emu/g) versus the CoFeB (Ms: 7.98 emu/g) NPs. This is attributed to the diamagnetic contribution from the Au cores. It is well established that the magnetic properties of NPs can be strongly affected by structural distortions at the surfaces and interfaces, as well as their structural order and disordered spins.<sup>90</sup> In the cases of synthesized Au@CoFeB NPs, these effects become more distinct. Furthermore, a large bias appeared in the Au@CoFeB NPs, which can be explained by the interactions between the ordered spins of the CoFeB shells, and the disordered spins located in the CoFeB/Au interfaces and outer surfaces of the CoFeB shells. Notably, after the modification and conjugation processes, the  $T_b$  for the Au@CoFeB-Rg3 NMs decreases, and their coercivity is increased. This is mainly attributed to the effective isolation of magnetic shells by drug molecules and reduction of magnetic dipole interactions among magnetic particles.

**Optical Imaging, MRI Imaging, and CT Imaging Applications.** LSPR colors of Au@CoFeB NPs and Au@CoFeB-Rg3 NMs were observed using dark-field microscopy. As shown in Figure 4a-i and b-i, the blue-green color for the Au@CoFeB NPs turns to the yellow-green for the Au@CoFeB-Rg3 NMs. According to the peak position statistics of the LSPR spectra of 50 randomly selected particles, Au@CoFeB-Rg3 particles exhibit red-shifts by approximately 36 nm after the surface modification and the conjugation process. The typical LSPR spectra of the single Au@CoFeB NPs and single Au@CoFeB-Rg3 NMs (i.e., bright spots in Figure 4a-i and b-i) are shown in Figure 4a-ii and b-ii, respectively. As shown in their LSPR spectra, after surface modification and conjugation with Rg3, the spectrum becomes broader and exhibits a clear red shift for the Au@CoFeB-Rg3 NMs. This effect is attributed to further alterations in the environment of the Au cores. Investigation of the plasmonic properties of Au@CoFeB NPs and Au@CoFeB-Rg3 NMs provides an experimental LSPR probe of the nanoparticle surrounding. Moreover, in some cases, it also extends potential uses as components in a diverse range of ultrasensitive chemical/biological sensors. Compared with the fluorescence dyes and the quantum dots,<sup>91,92</sup> which have to be excited by strong lasers and usually suffer from photobleaching, these metallic NPs can be easily used as an optical bioprobe for long-term tracking of the interactions between cell and cell, as well as cell and biomolecule/medicine under white light using dark-field microscopy. This also avoids the phototoxicity to the living cells.<sup>93–95</sup> These metallic NPs are easily conjugated with biomolecules and medicines using our invented amino-silane combined DSS coupling reaction methods, which result in the markedly enhanced stability

comparing to those of the traditional dye-based probes or quantum dots excited by lasers at certain wavelengths that are usually harmful to living cells under direct long-term irradiation.

Our previous investigation demonstrated that magnetic  $\text{Fe}_3\text{O}_4$  NPs can be used as MRI contrast enhancers by greatly improving alternations of proton relaxation in the tissue environment.<sup>96</sup> Therefore, considering the unique magnetic properties of the Au@CoFeB NPs and Au@CoFeB-Rg3 NMs, apart from the aforementioned optical imaging application, we further extended them to the clinical application as contrast agents for MRI and CT imaging. Owing to its noninvasiveness, high spatial resolution, and tissue-sensitive advantages, molecular imaging is applicable to the diagnosis of numerous diseases (e.g., cancer, neurological, and cardiovascular diseases), enabling the visualization of the cellular function in living organisms.<sup>47,97</sup> Among the molecular imaging technologies, MRI is used for the morphological and functional imaging of the anatomy and physiological processes of the body. On the basis of the relaxation and biocompatibility in the imaging process,<sup>98,99</sup> appropriate MRI contrast agents are much required to realize high specificity. Thus, the MRI effects of Au@CoFeB and Au@CoFeB-Rg3 were evaluated. The effective-metal (Co and Fe) concentration-dependent  $T_2$ -weighted spin-echo imaging effects and the corresponding  $T_2$  relaxation rates of Au@CoFeB NPs (Figure 4c:  $T_2^{-1}$ ) and Au@CoFeB-Rg3 (Figure 4d:  $T_2^{-1}$ ) are also shown in Figure 4. It is demonstrated that their MRI images exhibit very high signal intensities in the  $T_2$ -weighted image (top images in Figure 4c and d). These dual-mode MRI effects with high-sensitivity are caused by the combined effects of the unique magnetic properties and surface properties of the NPs. Additionally, their  $T_2$  relaxations exhibit a perfect linear relationship with their concentration, having the linear coefficients of 0.978 and 0.998 for Au@CoFeB NPs and Au@CoFeB-Rg3 NMs, respectively. Furthermore, the  $T_2$  relaxation rates (slopes) are about  $0.132 (\mu\text{g-CoFe mL}^{-1})^{-1} \text{ s}^{-1}$  and  $0.430 (\mu\text{g-CoFe mL}^{-1})^{-1} \text{ s}^{-1}$  for Au@CoFeB NPs and Au@CoFeB-Rg3 NMs, respectively. These values are markedly higher than that of commercial gadopentetate dimeglumine ( $0.025 (\mu\text{g-Gd mL}^{-1})^{-1} \text{ s}^{-1}$ ) reported in our previous research.<sup>40</sup> In addition, the combination of MRI and CT strategies can achieve a highly accurate diagnosis of disease, by providing complementary diagnostic information.<sup>100</sup> Therefore, the utilization of Au@CoFeB NPs as a dual contrast agent in CT imaging, which can exhibit excellent imaging details, was further investigated. Figure 4e shows the CT signal intensity of Au@CoFeB-Rg3 NMs with different concentrations, demonstrating a linear increase from 136 to 261 HU in response to an increased concentration of the contrast agent (400–4,000  $\mu\text{g/mL}$ ), whose linearly dependent coefficient is approximately 0.983. These results indicate that the Au@CoFeB-Rg3 NMs can be multimode clinical nanomedicines, which have the potential to permit MRI or CT imaging and tracing nanomedicines at the three-dimensional depth within tissues or opaque organisms at an enhanced resolution, possibly up to the nanoscale.

**Cell Viability Analysis.** The cytotoxicity and antitumor effects of the Au@CoFeB NPs and Au@CoFeB-Rg3 NMs were evaluated for a future *in vivo* animal study and final clinical applications. Without a loss of generality, 3T3 cells and Jurkat-CT cells were selected as healthy cell models, while K562-CT cells and Hep-G2/C3A cells were chosen as tumor

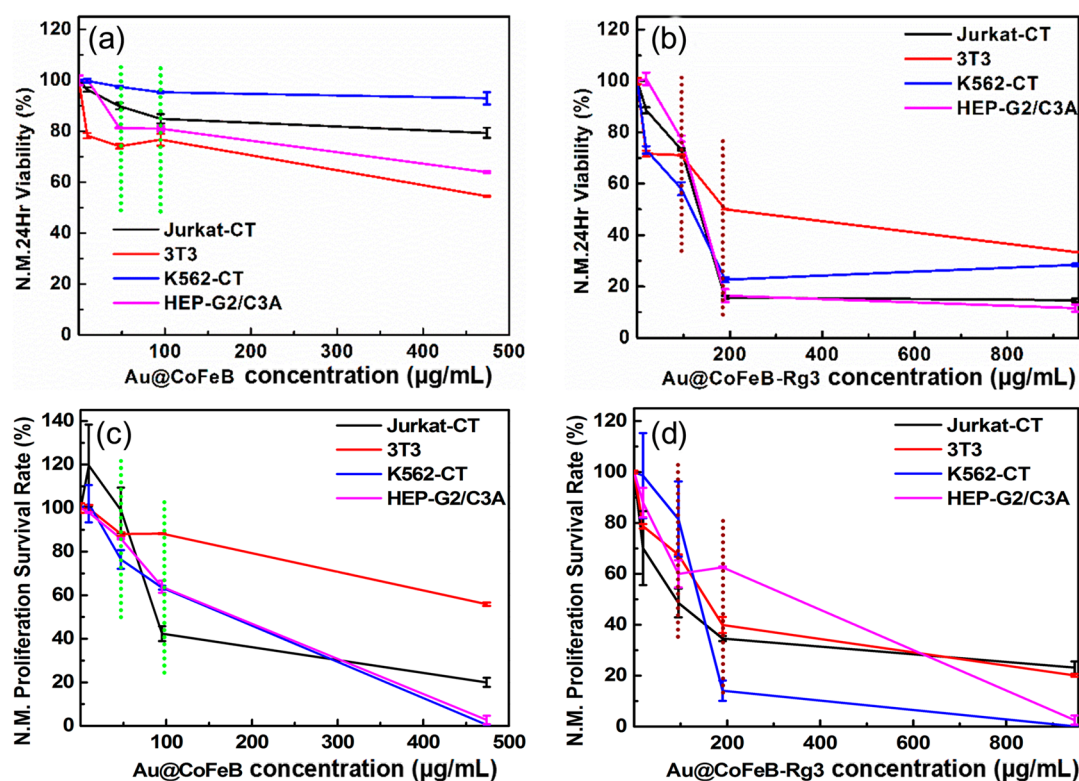


**Figure 5.** (a) Au@CoFe(B) and (b) Au@CoFe(B)-Rg3 concentration-dependent normalized (NM) 24 h viabilities and (c) Au@CoFe(B) and (d) Au@CoFe(B)-Rg3 concentration-dependent NM 4-day proliferation survival rates of Jurkat-CT cells (black curve), 3T3 cells (red curve), K562-CT cells (blue curve), and HEP-G2/C3A cells (pink curve).

cell models. The selection of these cells was based on the following reasons. 3T3 cells, belonging to the vascular epithelial cells, are often used in the cultivation of keratinocytes and can secrete (more vascular permeability factors in tumor tissues than the healthy tissues) growth factors favorable to these kinds of cells. Conventionally, this kind of cell is treated *via* the injection method, and the drugs must pass through these cells to target the solid tumors. Thus, the toxicity to such healthy cells warrants investigation. Moreover, these cells are also required for the growth of solid tumors and angiogenesis. Therefore, the effect on these cells directly affects whether the tumor sites can be used to enhance permeation and retention effects to transport more drugs to the tumor and even to deep tissues. Jurkat-CT cells are a kind of immune T cell that generally exist as suspension cells in the blood. K562-CT cells are a kind of human chronic myeloid leukemia cancer cell that exist as suspension cells in the blood. Hep-G2/C3A cells are a kind of hepatocellular cell, which are adherent and can become a solid tumor.

The cytotoxicity data show that Au@CoFe(B) NPs at concentrations  $< 95 \mu\text{g/mL}$  have low toxicity to all types of cells (Figure 5a), indicating that these NPs can be used as nanoprobes (optical nanoprobes, magnetic nanoprobes, and C-ray nanoprobes) for observation within 24 h. However, owing to their inhibition effect on cell proliferation (Figure 5c), it is preferable to use these NPs as nanoprobes at concentrations  $\leq 47 \mu\text{g/mL}$  for observation of longer duration (i.e., 4 days). At higher concentrations (e.g.,  $474 \mu\text{g/mL}$ ), the NPs induce marked toxicity to 3T3 cells and Hep-G2/C3A cells but not to Jurkat-CT cells and K562-CT cells. This result suggests that the NPs are more toxic to adherent cells that can be grown on tissues than to suspension cells. However, at high concen-

trations, they show significant inhibitory effects on these cells, especially for cancer cells (i.e., K562-CT and Hep-G2/C3A). Surprisingly, at a concentration of  $47 \mu\text{g/mL}$ , the NPs inhibit the proliferation of K562-CT and Hep-G2/C3A cells more than that of Jurkat-CT cells (Figure 5c). Especially for concentrations  $< 95 \mu\text{g/mL}$ , this type of nanoprobes can even enhance the proliferation of Jurkat-CT cells, which can be potentially used to enhance the effect of immunotherapy at low concentrations.

The cytotoxicity suggests that Au@CoFe(B)-Rg3 NMs, at a concentration of  $< 95 \mu\text{g/mL}$  (having Au@CoFe(B) NPs of  $47 \mu\text{g/mL}$ ), are associated with low toxicity to all cells, except K562-CT (Figure 5b). This means that Au@CoFe(B)-Rg3 can also be used as nanoprobes for 3T3, Hep-G2/C3A, and Jurkat cells at a certain low concentration. By comparing the cytotoxicity of Au@CoFe(B)-Rg3 with that of Au@CoFe(B), it is clear that conjugation of Rg3 to NHs for the formation of NMs can increase the toxicity to cells. Particularly, even at a low concentration of  $95 \mu\text{g/mL}$ , the NM for K562 showed marked toxicity. At concentrations  $> 190 \mu\text{g/mL}$ , the NM also shows significant toxicity to Hep-G2/C3A and Jurkat-CT cells. For cancer cells K562 and Hep-G2/C3A, the NMs at concentrations  $> 195 \mu\text{g/mL}$  show good therapeutic effects. This kind of NM can also be used for the design of a combined cancer therapy, particularly for those cancers involving Hep-G2/C3A cells. However, based on the results, it is recommended not to use such NMs simultaneously with immunotherapy (e.g., programmed death-1, programmed death-ligand 1, chimeric antigen receptor T). However, they may be suitable for use after the completion of immunotherapy to strengthen or consolidate their therapeutic effect. Interestingly, this kind of NM has the potential to be used in



combination with immunotherapy against some blood cancers of the erythroleukemia type.

Considering the results shown in Figure 5b and d, it is clear that the high concentration of Au@CoFe(B)-Rg3 exerts an excellent cytotoxic effect against cancer cells, as well as significant inhibition of proliferation for both suspension cancer cells (i.e., K562) and adherent cancer cells (i.e., Hep-G2/C3A). Particularly, according to the results of the cytotoxicity analysis, this type of NM may induce marked therapeutic effects against blood cancers involving adherent cells even at a relatively low concentration (195  $\mu\text{g/mL}$ ; Figure 5b) and inhibit the proliferation of K562 cells (Figure 5d). Despite the excellent cytotoxic effect of Au@CoFeB-Rg3 against Hep-G2/C3A within 24 h (Figure 5b), the long-term inhibitory effect on proliferation is not satisfactory at low concentrations (e.g., 190  $\mu\text{g/mL}$ ) much lower than the effect observed for K562 (Figure 5d). Hep-G2/C3A cells may be more diverse than K562 cells. Another possibility is the presence of super Hep-G2/C3A cells exhibiting greater viability than common Hep-G2/C3A cells. Thus, even though most of the common Hep-G2/C3A cells and many of the super Hep-G2/C3A cells can be killed within the first 24 h at low concentrations, the super Hep-G2/C3A cells may remain alive and proliferate in the long term treatment of NMs at low concentrations, showing a viable cell percentage  $\leq 63\%$ , relative to the control group at the concentration of 190  $\mu\text{g/mL}$  (Figure 5d). At high concentrations, even though most of the super Hep-G2/C3A cells cannot be immediately killed at the initiation of treatment with NMs, their routine cell functions could be drastically affected, leading to enhanced apoptosis of these supercells. This result suggests that the concentration of NMs may have to be increased to 947  $\mu\text{g/mL}$  for excellent therapeutic effects against solid tumors.

## CONCLUSION

A simple, rapid, and feasible sequenced temperature-programmed microfluidic process combining surface modification and functionalization of nanohybrids was developed to prepare nanomedicines (e.g., Au@CoFeB-Rg3) with multi-mode imaging functions and excellent antitumor effects. These NMs can be visually traced via dark-field microscopy and spectroscopy owing to the localized surface plasmon of the Au cores. Moreover, they can be traced through MRI and CT imaging owing to the superparamagnetic property of CoFeB shells at room temperature and the strong interaction with X-ray radiation. These functions render the diagnosis more accurate and visible in both in vitro cell studies and in vivo tissue/organ studies for the final clinical application. Additionally, Au@CoFeB NPs and Au@CoFeB-Rg3 NMs exhibit excellent antitumor effects or can be used to distinctly kill cancer cells and inhibit the proliferation of cancer cells. Notably, they also have a low cytotoxicity to 3T3 cells. It is concluded that these magneto-plasmonic core-shell NPs could potentially permit flexibility in the tuning of magnetic and optical properties and interaction with X-ray radiation for future clinical applications in molecule imaging and cancer therapy. The in vivo antitumor effects of these NMs using orthotopic hepatocarcinoma mice as an animal model are currently under evaluation. These NMs can play a role as clinically visible NMs that can be guided to the target using a magnetic field and traced through MRI and/or CT imaging at an enhanced special resolution for long-term function evaluation of nanomedicines. A previous study revealed the

self-richness of Fe-based NMs in livers. Therefore, besides their intrinsic role as antitumor agents, these NMs can also be used in magnetic/photobased and radio frequency-based therapy, particularly for the treatment of hepatocarcinoma, since they have self-enrichment in livers based on our previous study on Fe-based NMs.<sup>101</sup> All of these studies are under progress and will be published soon.

## ASSOCIATED CONTENT

### Supporting Information

The Supporting Information is available free of charge at <https://pubs.acs.org/doi/10.1021/acs.chemmater.0c00797>.

The synthesis of the CoFeB NPs using a simple programed microfluidic process; synthesis of the Au@CoFeB-Rg3 NMs; characterization of the structure, composition, zeta potential, and hydrodynamic radius; characterization of localized surface plasmon resonance and magnetic properties; characterization of magnetic properties and related MIR and CT effects; and cell viability assay (PDF)

## AUTHOR INFORMATION

### Corresponding Author

**Yujun Song** – Center for Modern Physics Technology, School of Mathematics and Physics, University of Science and Technology Beijing, Beijing 100083, China; Physics Department, School of Engineering and Applied Science, Harvard University, Cambridge, Massachusetts 02138, United States; Zhengzhou Tianzhao Biotechnology Company, Ltd., Zhengzhou 451450, China; School of Materials Science and Engineering, Beihang University, Beijing 100091, China; [orcid.org/0000-0003-2474-084X](https://orcid.org/0000-0003-2474-084X); Email: [songyj@ustb.edu.cn](mailto:songyj@ustb.edu.cn)

### Authors

**Weiwei Zhang** – Center for Modern Physics Technology, School of Mathematics and Physics, University of Science and Technology Beijing, Beijing 100083, China; Zhengzhou Tianzhao Biotechnology Company, Ltd., Zhengzhou 451450, China; [orcid.org/0000-0002-9083-8290](https://orcid.org/0000-0002-9083-8290)

**Xiaoxiong Zhao** – Center for Modern Physics Technology, School of Mathematics and Physics, University of Science and Technology Beijing, Beijing 100083, China; Zhengzhou Tianzhao Biotechnology Company, Ltd., Zhengzhou 451450, China

**Yuan Yuan** – Physics Department, School of Engineering and Applied Science, Harvard University, Cambridge, Massachusetts 02138, United States

**Fenglin Miao** – Department of Hepatobiliary Surgery, Xiang'an Hospital of Xiamen University, School of Medicine, Xiamen 361102, China

**Wengang Li** – Department of Hepatobiliary Surgery, Xiang'an Hospital of Xiamen University, School of Medicine, Xiamen 361102, China

**Shaoxia Ji** – School of Materials Science and Engineering, Beihang University, Beijing 100091, China

**Xing Huang** – Physics Department, School of Engineering and Applied Science, Harvard University, Cambridge, Massachusetts 02138, United States

**Xinhua Chen** – Key Laboratory of Combined Multiorgan Transplantation, Ministry of Public Health, Department of Hepatobiliary and Pancreatic Surgery, the First Affiliated

Hospital, Zhejiang University, Hangzhou, Zhejiang 310003, China

**Tianan Jiang** – Key Laboratory of Combined Multiorgan Transplantation, Ministry of Public Health, Department of Hepatobiliary and Pancreatic Surgery, the First Affiliated Hospital, Zhejiang University, Hangzhou, Zhejiang 310003, China

**David A. Weitz** – Physics Department, School of Engineering and Applied Science, Harvard University, Cambridge, Massachusetts 02138, United States; [orcid.org/0000-0001-6678-5208](https://orcid.org/0000-0001-6678-5208)

Complete contact information is available at:

<https://pubs.acs.org/10.1021/acs.chemmater.0c00797>

## Author Contributions

†Contributed to this article equally. All authors have given approval to the final version of the manuscript.

## Funding

This study was financially supported by the National Natural Science Foundation of China (no. 51971029), National S&T Major Project of China (no. 2018ZX10301201), the BRICS STI Framework Programmed by NSFC (no. 51861145309), the China Scholarship Council (awarded to Y.S. for one and a half years' study abroad at Harvard University, no. 201706465051), the "1125" Zhihui Zhengzhou Talent project of Henan province (fund no. in USTB: 39080070), and the "100 talent plan" fund of Fujian province (fund no. in USTB: 39080067), and the development of a highly sensitive magneto-optical biomolecular sensor experimental prototype (fund no. in USTB: 2019-0649) was funded by Hangzhou Ruidi Biotechnology Co., Ltd.

## Notes

The authors declare no competing financial interest.

## ACKNOWLEDGMENTS

Y.S. appreciates Wen Han at Harvard University for the cell culture training.

## REFERENCES

- (1) Tekade, R.; Maheshwari, R.; Soni, N.; Tekade, M.; Chougule, M. *Nanotechnology-Based Approaches for Targeting and Delivery of Drugs and Genes*; Elsevier: Amsterdam, 2017; pp 3–61.
- (2) Mody, N.; Tekade, R. K.; Mehra, N. K.; Chopdey, P.; Jain, N. K. Dendrimer, Liposomes, Carbon Nanotubes and PLGA Nanoparticles: One Platform Assessment of Drug Delivery Potential. *AAPS PharmSciTech* **2014**, 15 (2), 388–399.
- (3) Alhareth, K.; Sancey, L.; Tsapis, N.; Mignet, N. How should we plan the future of nanomedicine for cancer diagnosis and therapy? *Int. J. Pharm.* **2017**, 532 (2), 657–659.
- (4) Bhise, K.; Sau, S.; Alsaab, H.; Kashaw, S. K.; Tekade, R. K.; Iyer, A. K. Nanomedicine for cancer diagnosis and therapy: advancement, success and structure-activity relationship. *Ther. Delivery* **2017**, 8 (11), 1003–1018.
- (5) El-Zahaby, S. A.; Elnaggar, Y. S. R.; Abdallah, O. Y. Reviewing two decades of nanomedicine implementations in targeted treatment and diagnosis of pancreatic cancer: An emphasis on state of art. *J. Controlled Release* **2019**, 293, 21–35.
- (6) Ladju, R. B.; Pascut, D.; Massi, M. N.; Tiribelli, C.; Sukowati, C. H. C. Aptamer: A potential oligonucleotide nanomedicine in the diagnosis and treatment of hepatocellular carcinoma. *Oncotarget* **2018**, 9 (2), 2951–2961.
- (7) Ladju, R. B.; Pascut, D.; Massi, M. N.; Tiribelli, C.; Sukowati, C. H. C. Correction: Aptamer: A potential oligonucleotide nano-

medicine in the diagnosis and treatment of hepatocellular carcinoma. *Oncotarget* **2018**, 9 (16), 13101–13101.

(8) Lee, H.; Jang, Y.; Park, S.; Jang, H.; Park, E.-J.; Kim, H. J.; Kim, H. Development and evaluation of a CEACAM6-targeting theranostic nanomedicine for photoacoustic-based diagnosis and chemotherapy of metastatic cancer. *Theranostics* **2018**, 8 (15), 4247–4261.

(9) Ushenko, Y. A.; Syvokorovskaya, A. V.; Gorsky, M. P.; Tomka, Y. Y.; Bakun, O.; Kvasnuyk, D.; Kushnerik, L. Y.; Golub, S.; Besaga, R., Digital polarization-holographic 3D reconstruction of the polycrystalline structure of blood films in the diagnosis of breast cancer. In *Biosensing and Nanomedicine XI*; Mohseni, H., Agahi, M. H., Razeghi, M., Eds.; SPIE, 2018; vol. 10728.

(10) Xu, J.; Liao, K.; Jiang, H.; Zhou, W. Research progress of novel inorganic nanometre materials carriers in nanomedicine for cancer diagnosis and treatment. *Artif. Cells, Nanomed., Biotechnol.* **2018**, 46, S492–S502.

(11) Zhang, T.; Zhang, Q.; Tian, J.-H.; Xing, J.-F.; Guo, W.; Liang, X.-J. Perfluorocarbon-based nanomedicine: emerging strategy for diagnosis and treatment of diseases. *MRS Commun.* **2018**, 8 (2), 303–313.

(12) Mansuri, S.; Kesharwani, P.; Tekade, R. K.; Jain, N. K. Lyophilized mucoadhesive-dendrimer enclosed matrix tablet for extended oral delivery of albendazole. *Eur. J. Pharm. Biopharm.* **2016**, 102, 202–213.

(13) Al-Lawati, H.; Binkhathlan, Z.; Lavasanifar, A. Nanomedicine for the effective and safe delivery of non-steroidal anti-inflammatory drugs: A review of preclinical research. *Eur. J. Pharm. Biopharm.* **2019**, 142, 179–194.

(14) Meng, T.; Kulkarni, V.; Simmers, R.; Brar, V.; Xu, Q. Therapeutic implications of nanomedicine for ocular drug delivery. *Drug Discovery Today* **2019**, 24 (8), 1524–1538.

(15) Pearce, A. K.; O'Reilly, R. K. Insights into Active Targeting of Nanoparticles in Drug Delivery: Advances in Clinical Studies and Design Considerations for Cancer Nanomedicine. *Bioconjugate Chem.* **2019**, 30 (9), 2300–2311.

(16) Peng, F.; Zhang, W.; Qiu, F. Self-assembling Peptides in Current Nanomedicine: Versatile Nanomaterials for Drug Delivery. *Curr. Med. Chem.* **2019**, 26 (1), 1–26.

(17) Neacșu, I. A.; Nicoară, A. I.; Vasile, O. R.; Vasile, B. Ș. Chapter 9 - Inorganic micro- and nanostructured implants for tissue engineering **2016**, 4, 271–295.

(18) Bayindir-Buchhalter, I.; Gobel, U.; Stimson, L. Biofabrication, Biomedical Devices, Nanomedicine, and Tissue Engineering - Advanced Materials in Healthcare. *Adv. Healthcare Mater.* **2018**, 7 (1), 1701399.

(19) Hu, E.; Bayindir-Buchhalter, I.; Goebel, U. Nanomedicine, Biofabrication, Tissue Engineering and Much More - Advanced Healthcare Materials Welcomes 2019. *Adv. Healthcare Mater.* **2019**, 8 (1), 1801576.

(20) Izadifar, M.; Kelly, M. E.; Chen, X. Computational nanomedicine for mechanistic elucidation of bilayer nanoparticle-mediated release for tissue engineering. *Nanomedicine* **2017**, 12 (5), 423–441.

(21) Hock, S. C.; Ying, Y. M.; Wah, C. L. A review of the current scientific and regulatory status of nanomedicines and the challenges ahead. *Pda J. Pharmaceutical Sci. Technol.* **2011**, 65 (2), 177.

(22) Germain, M.; Poul, L.; Meyre, M.-E.; Paolini, M.; Mpambani, F.; Bergere, M.; Pottier, A.; Levy, L. Redefine nanomedicine products bioavailability to improve antitumor efficacy. *Cancer Res.* **2018**, 78 (13), LB-072.

(23) Ravindran, S.; Tambe, A. J.; Suthar, J. K.; Chahar, D. S.; Fernandes, O. M.; Desai, V. Nanomedicine: Bioavailability, Biotransformation and Biokinetics. *Curr. Drug Metab.* **2019**, 20 (7), 542–555.

(24) Boisseau, P.; Loubaton, B. Nanomedicine, nanotechnology in medicine. *C. R. Phys.* **2011**, 12 (7), 620–636.

(25) Attari, Z.; Bhandari, A.; Jagadish, P. C.; Lewis, S. Enhanced ex vivo intestinal absorption of olmesartan medoxomil nanosuspension: Preparation by combinative technology. *Saudi Pharm. J.* **2016**, 24 (1), 57–63.

- (26) Azimi, B.; Nourpanah, P.; Rabiee, M.; Arbab, S. Producing gelatin nanoparticles as delivery system for bovine serum albumin. *Iranian Biomedical Journal* **2013**, *18* (1), 34–40.
- (27) Rampino, A.; Borgogna, M.; Blasi, P.; Bellich, B.; Cesàro, A. Chitosan nanoparticles: Preparation, size evolution and stability. *Int. J. Pharm.* **2013**, *455* (1), 219–228.
- (28) Kumari, A.; Yadav, S. K.; Yadav, S. C. Biodegradable polymeric nanoparticles based drug delivery systems. *Colloids Surf., B* **2010**, *75* (1), 1–18.
- (29) Mahmoudi, M.; Sant, S.; Wang, B.; Laurent, S.; Sen, T. Superparamagnetic iron oxide nanoparticles (SPIONs): Development, surface modification and applications in chemotherapy. *Adv. Drug Delivery Rev.* **2011**, *63* (1), 24–46.
- (30) Wei, L.; Lu, J.; Xu, H.; Patel, A.; Chen, Z.-S.; Chen, G. Silver nanoparticles: synthesis, properties, and therapeutic applications. *Drug Discovery Today* **2015**, *20* (5), 595–601.
- (31) Zhou, W.; Gao, X.; Liu, D.; Chen, X. Gold Nanoparticles for In Vitro Diagnostics. *Chem. Rev.* **2015**, *115* (19), 10575–10636.
- (32) Wang, Y.; Hu, A. Carbon quantum dots: synthesis, properties and applications. *J. Mater. Chem. C* **2014**, *2*, 6921.
- (33) Tekade, R. K.; Kumar, P. V.; Jain, N. K. Dendrimers in Oncology: An Expanding Horizon. *Chem. Rev.* **2010**, *110* (4), 2574.
- (34) Bozzuto, G.; Molinari, A. Liposomes as nanomedical devices. *Int. J. Nanomed.* **2015**, *10* (1), 975–999.
- (35) Kawasaki, E. S.; Player, A. Nanotechnology, nanomedicine, and the development of new, effective therapies for cancer. *Nanomedicine* **2005**, *1* (2), 101–109.
- (36) Cencini, E.; Sicuranza, A.; Fabbri, A.; Ferrigno, I.; Rigacci, L.; Cox, M. C.; Raspadori, D.; Bocchia, M. Study of gene polymorphisms as predictors of treatment efficacy and toxicity in patients with indolent non-hodgkin lymphomas and mantle cell lymphoma receiving bendamustine and rituximab. *Br. J. Haematol.* **2019**, *184* (2), 223–231.
- (37) Wang, S.; Niu, S. Y.; Li, H. S.; Lam, K. K.; Wang, Z. R.; Du, P. Y.; Leung, C. W.; Qu, S. X. Synthesis and controlled morphology of Ni@Ag core shell nanowires with excellent catalytic efficiency and recyclability. *Nanotechnology* **2019**, *30* (38), 385603.
- (38) Maiti, K.; Balamurugan, J.; Peera, S. G.; Kim, N. H.; Lee, J. H. Highly Active and Durable Core-Shell fct-PdFe@Pd Nanoparticles Encapsulated NG as an Efficient Catalyst for Oxygen Reduction Reaction. *ACS Appl. Mater. Interfaces* **2018**, *10* (22), 18734–18745.
- (39) Anderson, S. D.; Gwenin, V. V.; Gwenin, C. D. Magnetic Functionalized Nanoparticles for Biomedical, Drug Delivery and Imaging Applications. *Nanoscale Res. Lett.* **2019**, *14* (1), 188.
- (40) Wang, J. M.; Zhao, K.; Shen, X. M.; Zhang, W. W.; Ji, S. X.; Song, Y. J.; Zhang, X. D.; Rong, R.; Wang, X. Y. Microfluidic synthesis of ultra-small magnetic nanohybrids for enhanced magnetic resonance imaging. *J. Mater. Chem. C* **2015**, *3* (48), 12418–12429.
- (41) Morales-Kastresana, A.; Musich, T. A.; Welsh, J. A.; Telford, W.; Demberg, T.; Wood, J. C. S.; Bigos, M.; Ross, C. D.; Kachynski, A.; Dean, A.; Felton, E. J.; Van Dyke, J.; Tigges, J.; Toxavidis, V.; Parks, D. R.; Overton, W. R.; Kesarwala, A. H.; Freeman, G. J.; Rosner, A.; Perfetto, S. P.; Pasquet, L.; Terabe, M.; McKinnon, K.; Kapoor, V.; Trepel, J. B.; Puri, A.; Kobayashi, H.; Yung, B.; Chen, X.; Guion, P.; Choyke, P.; Knox, S. J.; Ghiran, I.; Robert-Guroff, M.; Berzofsky, J. A.; Jones, J. C. High-fidelity detection and sorting of nanoscale vesicles in viral disease and cancer. *J. Extracell. Vesicles* **2019**, *8* (1), 1597603.
- (42) Santos, G. S.; Caldas, R. G. S. C.; Melo, F. L.; Bruscky, I. S.; Silva, M. A. L.; Wanderley, L. B.; Andrade, C. A. S.; Oliveira, M. D. L. Label-free nanostructured biosensor for *Schistosoma mansoni* detection in complex biological fluids. *Talanta* **2019**, *204* (1), 395–401.
- (43) Gan, H. Y.; Wu, J.; Ju, H. X. Proximity hybridization-induced on particle DNA walker for ultrasensitive protein detection. *Anal. Chim. Acta* **2019**, *1074* (3), 142–149.
- (44) Kwizera, E. A.; Chaffin, E.; Wang, Y. M.; Huang, X. H. Synthesis and properties of magnetic-optical core-shell nanoparticles. *RSC Adv.* **2017**, *7* (28), 17137–17153.
- (45) Chen, H.; Liu, F.; Lei, Z.; Ma, L.; Wang, Z. Fe<sub>2</sub>O<sub>3</sub>@Au Core@Shell Nanoparticle-Graphene Nanocomposites as Theranostic Agents for Bioimaging and Chemo-Photothermal Synergistic Therapy. *RSC Adv.* **2015**, *5* (103), 84980–84987.
- (46) Zhang, W.; Wang, Q.; Zhao, C.; Song, Y. The optical cavity enhanced magneto-optical Kerr effect signals of AAO/Al-based CoFeB nanostructure arrays. *Opt. Commun.* **2019**, *437* (15), 44–49.
- (47) Song, Y.; Wang, R.; Rong, R.; Ding, J.; Liu, J.; Li, R.; Liu, Z.; Li, H.; Wang, X.; Zhang, J.; Fang, J. Synthesis of Well-Dispersed Aqueous-Phase Magnetite Nanoparticles and Their Metabolism as an MRI Contrast Agent for the Reticuloendothelial System. *Eur. J. Inorg. Chem.* **2011**, *2011* (22), 3303–3313.
- (48) Wang, J.; Wang, Z.; Li, S.; Wang, R.; Song, Y. Surface and interface engineering of FePt/C nanocatalysts for electro-catalytic methanol oxidation: enhanced activity and durability. *Nanoscale* **2017**, *9* (12), 4066–4075.
- (49) Esmaeili, E.; Khalili, M.; Sohi, A. N.; Hosseinzadeh, S.; Taheri, B.; Soleimani, M. Dendrimer functionalized magnetic nanoparticles as a promising platform for localized hyperthermia and magnetic resonance imaging diagnosis. *J. Cell. Physiol.* **2019**, *234* (8), 12615–12624.
- (50) Vu-Quang, H.; Vinding, M. S.; Nielsen, T.; Ullisch, M. G.; Nielsen, N. C.; Nguyen, D.-T.; Kjems, J. Pluronic F127-Folate Coated Super Paramagnetic Iron Oxide Nanoparticles as Contrast Agent for Cancer Diagnosis in Magnetic Resonance Imaging. *Polymers* **2019**, *11* (4), 743.
- (51) Kim, S.; Jeong, S. H.; Song, J.; Lee, W. Fluorescent nanoparticles used in photoluminescent material for diagnosis or imaging of tumor, contains peptide moiety, spacer moiety for improving enzyme accessibility, and charge-bearing moiety including molecular sieve. Patent KR KR2019015685-A, 2019.
- (52) Mirahadi, M.; Ghanbarzadeh, S.; Ghorbani, M.; Gholizadeh, A.; Hamishehkar, H. A review on the role of lipid-based nanoparticles in medical diagnosis and imaging. *Ther. Delivery* **2018**, *9* (8), 557–569.
- (53) Leon Felix, L.; Coaquira, J. A.; Martinez, M. A.; Goya, G. F.; Mantilla, J.; Sousa, M. H.; Valladares, L. L.; Barnes, C. H.; Morais, P. C. Structural and magnetic properties of core-shell Au/Fe<sub>3</sub>O<sub>4</sub> nanoparticles. *Sci. Rep.* **2017**, *7* (1), 41732.
- (54) Wang, J.; Song, Y. Microfluidic Synthesis of Nanohybrids. *Small* **2017**, *13* (18), 1604084.
- (55) Chan, K. K.; Yap, S. H. K.; Yong, K.-T. Biogreen Synthesis of Carbon Dots for Biotechnology and Nanomedicine Applications. *Nano-Micro Lett.* **2018**, *10* (4), 72.
- (56) Couvreur, P.; Stella, B.; Reddy, L. H.; Hillaireau, H.; Dubernet, C.; Desmaele, D.; Lepetre-Mouelhi, S.; Rocco, F.; Dereuddre-Bosquet, N.; Clayette, P.; Rosilio, V.; Marsaud, V.; Renoir, J.-M.; Cattel, L. Squalenoyl Nanomedicines as Potential Therapeutics. *Nano Lett.* **2006**, *6* (11), 2544–2548.
- (57) Khopade, A. J.; Caruso, F. Electrostatically Assembled Polyelectrolyte/Dendrimer Multilayer Films as Ultrathin Nano-reservoirs. *Nano Lett.* **2002**, *2* (4), 415–418.
- (58) Zhou, H.; Mu, Q.; Gao, N.; Liu, A.; Xing, Y.; Gao, S.; Zhang, Q.; Qu, G.; Chen, Y.; Liu, G.; Zhang, B.; Yan, B. A Nano-Combinatorial Library Strategy for the Discovery of Nanotubes with Reduced Protein-Binding, Cytotoxicity, and Immune Response. *Nano Lett.* **2008**, *8* (3), 859–865.
- (59) Lignos, I.; Protesescu, L.; Emiroglu, D. B.; Maceiczky, R.; Schneider, S.; Kovalenko, M. V.; deMello, A. J. Unveiling the Shape Evolution and Halide-Ion-Segregation in Blue-Emitting Formamidinium Lead Halide Perovskite Nanocrystals Using an Automated Microfluidic Platform. *Nano Lett.* **2018**, *18* (2), 1246–1252.
- (60) Liu, C.; Zhang, W.; Li, Y.; Chang, J.; Tian, F.; Zhao, F.; Ma, Y.; Sun, J. Microfluidic Sonication To Assemble Exosome Membrane-Coated Nanoparticles for Immune Evasion-Mediated Targeting. *Nano Lett.* **2019**, *19* (11), 7836–7844.
- (61) Xie, X.; Zhang, W.; Abbaspourrad, A.; Ahn, J.; Bader, A.; Bose, S.; Vegas, A.; Lin, J.; Tao, J.; Hang, T.; Lee, H.; Iverson, N.; Bisker, G.; Li, L.; Strano, M. S.; Weitz, D. A.; Anderson, D. G. Microfluidic



Fabrication of Colloidal Nanomaterials-Encapsulated Microcapsules for Biomolecular Sensing. *Nano Lett.* **2017**, *17* (3), 2015–2020.

(62) Ma, J.; Wang, J.; Zhong, X.; Li, G.; Song, Y. Synthesis of Sn(1-x)Fex@FeySn(1-y)Oz nanohybrids via a simple programmed microfluidic process. *RSC Adv.* **2016**, *6* (87), 84255–84261.

(63) Song, Y.; Ji, S.; Song, Y.-J.; Li, R.; Ding, J.; Shen, X.; Wang, R.; Xu, R.; Gu, X. In-situ Redox Microfluidic Synthesis of Core-Shell Nanoparticles and their Long-term Stability. *J. Phys. Chem. C* **2013**, *117* (33), 17274–17284.

(64) Liu, D.; Zhang, H.; Cito, S.; Fan, J.; Makila, E.; Salonen, J.; Hirvonen, J.; Sikanen, T. M.; Weitz, D. A.; Santos, H. A. Core/Shell Nanocomposites Produced by Superfast Sequential Microfluidic Nanoprecipitation. *Nano Lett.* **2017**, *17* (2), 606–614.

(65) Ma, J.; Wang, J.; Zhang, G.; Peng, L.; Song, X.; Ding, J.; Ji, S.; Song, Y. Magnetic and Optical Properties of Ag-CoFe Nanohybrids Prepared by a Sequenced Microfluidic Process. *Chemistry Select* **2019**, *4* (48), 14157–14161.

(66) Jiang, J.; Yuan, Z.; Sun, Y.; Bu, Y.; Li, W.; Fei, Z. Ginsenoside Rg3 enhances the anti-proliferative activity of erlotinib in pancreatic cancer cell lines by downregulation of EGFR/PI3K/Akt signaling pathway. *Biomed. Pharmacother.* **2017**, *96*, 619–625.

(67) Lee, J.-Y.; Jung, K. H.; Morgan, M. J.; Kang, Y.-R.; Lee, H.-S.; Koo, G.-B.; Hong, S.-S.; Kwon, S. W.; Kim, Y.-S. Sensitization of TRAIL-Induced Cell Death by 20(S)-Ginsenoside Rg3 via CHOP-Mediated DR5 Upregulation in Human Hepatocellular Carcinoma Cells. *Mol. Cancer Ther.* **2013**, *12* (3), 274–285.

(68) Shang, Q.; Xiao, E.; Zhong, H.; Tan, L.; Weijun, S.; Bao, M.; Yuan, S.; Du, W. Dynamic study of efficacy of transcatheter arterial chemoembolization (TACE) of primary liver carcinoma with the MR diffusion-weighted imaging (DWI). *Chinese Journal of Radiology* **2006**, *40* (3), 235–240.

(69) Jiang, J. W.; Chen, X. M.; Chen, X. H.; Zheng, S. S. Ginsenoside Rg3 inhibit hepatocellular carcinoma growth via intrinsic apoptotic pathway. *World Journal of Gastroenterology* **2011**, *17* (31), 3605–3613.

(70) Lee, D. C.; Lau, A. S. Effects of Panax ginseng on Tumor Necrosis Factor- $\alpha$ -Mediated Inflammation: A Mini-Review. *Molecules* **2011**, *16* (4), 2802–2816.

(71) Whitacre, D. M.; Bennett, E. R.; Doerge, D. R. Reviews of Environmental Contamination and Toxicology VOLUME 225 Foreword. In *Reviews of Environmental Contamination and Toxicology*; Whitacre, D. M., Ed.; Springer, 2013; Vol. 225, pp V–VI.

(72) Yang, H.; You, W.; Shen, Q.; Wang, X.; Sheng, J.; Cheng, D.; Cao, X.; Wu, C. Preparation of lotus-leaf-like antibacterial film based on mesoporous silica microcapsule-supported Ag nanoparticles. *RSC Adv.* **2014**, *4* (6), 2793–2796.

(73) Lin, J.; Zhou, W.; Kumbhar, A.; Wiemann, J.; Fang, J.; Carpenter, E. E.; O'Connor, C. J. Gold-Coated Iron (Fe@Au) Nanoparticles: Synthesis, Characterization, and Magnetic Field-Induced Self-Assembly. *J. Solid State Chem.* **2001**, *159* (1), 26–31.

(74) Zhao, X.; Wang, J.; Song, Y.; Chen, X. Synthesis of nanomedicines by nanohybrids conjugating ginsenosides with auto-targeting and enhanced MRI contrast for liver cancer therapy. *Drug Dev. Ind. Pharm.* **2018**, *44* (8), 1307–1316.

(75) Govorov, A. O.; Zhang, W.; Skeini, T.; Richardson, H.; Lee, J.; Kotov, N. A. Gold nanoparticle ensembles as heaters and actuators: melting and collective plasmon resonances. *Nanoscale Res. Lett.* **2006**, *1* (1), 84.

(76) Song, Y.; Ding, J.; Wang, Y. Shell-Dependent Evolution of Optical and Magnetic Properties of Co@Au Core-Shell Nanoparticles. *J. Phys. Chem. C* **2012**, *116* (20), 11343–11350.

(77) Eustis, S.; El-Sayed, M. A. Why gold nanoparticles are more precious than pretty gold: Noble metal surface plasmon resonance and its enhancement of the radiative and nonradiative properties of nanocrystals of different shapes. *Chem. Soc. Rev.* **2006**, *35* (3), 209–217.

(78) Shi, W. L.; Zeng, H.; Sahoo, Y.; Ohulchanskyy, T. Y.; Ding, Y.; Wang, Z. L.; Swihart, M.; Prasad, P. N. A general approach to binary and ternary hybrid nanocrystals. *Nano Lett.* **2006**, *6* (4), 875–881.

(79) Shevchenko, E. V.; Bodnarchuk, M. I.; Kovalenko, M. V.; Talapin, D. V.; Smith, R. K.; Aloni, S.; Heiss, W.; Alivisatos, A. P. Gold/Iron Oxide Core/Hollow-Shell Nanoparticles. *Adv. Mater.* **2008**, *20* (22), 4323–4329.

(80) Ghosh, S. K.; Pal, T. Interparticle coupling effect on the surface plasmon resonance of gold nanoparticles: From theory to applications. *Chem. Rev.* **2007**, *107* (11), 4797–4862.

(81) Kelly, K. L.; Coronado, E.; Zhao, L. L.; Schatz, G. C. The optical properties of metal nanoparticles: The influence of size, shape, and dielectric environment. *J. Phys. Chem. B* **2003**, *107* (3), 668–677.

(82) Khlebtsov, N. G.; Trachuk, L. A.; Mel'nikov, A. G. The effect of the size, shape, and structure of metal nanoparticles on the dependence of their optical properties on the refractive index of a disperse medium. *Opt. Spectrosc.* **2005**, *98* (1), 77–83.

(83) Velasco, V.; Muñoz, L.; Mazario, E.; Menéndez, N.; Herrasti, P.; Hernando, A.; Crespo, P. Chemically synthesized Au-Fe3O4 nanostructures with controlled optical and magnetic properties. *J. Phys. D: Appl. Phys.* **2015**, *48* (3), 035502.

(84) Song, Y.; Ding, J.; Wang, Y. Shell-Dependent Evolution of Optical and Magnetic Properties of Co@Au Core-Shell Nanoparticles. *J. Phys. Chem. C* **2012**, *116* (20), 11343–11350.

(85) Song, Y.; Jin, P.; Zhang, T. Microfluidic Synthesis of Fe Nanoparticles. *Mater. Lett.* **2010**, *64* (16), 1789–1792.

(86) Song, Y.; Ji, S.; Song, Y.-J.; Li, R.; Ding, J.; Shen, X.; Wang, R.; Xu, R.; Gu, X. In Situ Redox Microfluidic Synthesis of Core-Shell Nanoparticles and Their Long-Term Stability. *J. Phys. Chem. C* **2013**, *117* (33), 17274–17284.

(87) Wang, J.; Zhao, K.; Shen, X.; Zhang, W.; Ji, S.; Song, Y.; Zhang, X.; Rong, R.; Wang, X. Microfluidic synthesis of ultra-small magnetic nanohybrids for enhanced magnetic resonance imaging. *J. Mater. Chem. C* **2015**, *3* (48), 12418–12429.

(88) Song, Y.; Henry, L. L.; Yang, W. Stable amorphous cobalt nanoparticles formed by an in situ rapidly cooling microfluidic process. *Langmuir* **2009**, *25* (17), 10209–17.

(89) Shen, X.; Song, Y.; Li, S.; Li, R.; Ji, S.; Li, Q.; Duan, H.; Xu, R.; Yang, W.; Zhao, K.; Rong, R.; Wang, X. Spatiotemporal-resolved nanoparticle synthesis via simple programmed microfluidic processes. *RSC Adv.* **2014**, *4* (64), 34179–34188.

(90) Punnoose, A.; Magnone, H.; Seehra, M. S.; Bonevich, J. Bulk to nanoscale magnetism and exchange bias in CuO nanoparticles. *Phys. Rev. B: Condens. Matter Mater. Phys.* **2001**, *64* (17), 607–611.

(91) Lien, V. T. K.; Tan, P. M.; Hien, N. T.; Hoa, V. X.; Chi, T. T. K.; Truong, N. X.; Oanh, V. T. K.; Thuy, N. T. M.; Ca, N. X. Tunable photoluminescent Cu-doped CdS/ZnSe type-II core/shell quantum dots. *J. Lumin.* **2019**, *215*, 116627.

(92) Yu, J. S.; Kim, S. H.; Man, M. T.; Lee, H. S. Synthesis and dual-channel optical properties of Mn-doped ZnSe quantum dots. *Mater. Lett.* **2019**, *253* (15), 367–371.

(93) Song, Y.; Elsayed-Ali, H. E. Aqueous phase Ag nanoparticles with controlled shapes fabricated by a modified nanosphere lithography and their optical properties. *Appl. Surf. Sci.* **2010**, *256* (20), 5961–5967.

(94) Song, Y.; Zhang, Z.; Elsayed-Ali, H. E.; Wang, H.; Henry, L. L.; Wang, Q.; Zou, S.; Zhang, T. Identification of single nanoparticles. *Nanoscale* **2011**, *3* (1), 31–44.

(95) Xu, X. H. N.; Song, Y.; Nallathamby, P. *Probing Membrane Transport of Single Live Cells Using Single-Molecule Detection and Single Nanoparticle Assay*; John Wiley & Sons, Ltd, 2006; pp 41–70.

(96) Song, Y.; Wang, R.; Rong, R.; Ding, J.; Liu, J.; Li, R.; Liu, Z.; Li, H.; Wang, X.; Zhang, J.; Fang, J. Synthesis of Well-Dispersed Aqueous-Phase Magnetite Nanoparticles and Their Metabolism as an MRI Contrast Agent for the Reticuloendothelial System. *Eur. J. Inorg. Chem.* **2011**, *2011* (22), 3303–3313.

(97) Tang, W.; Zhen, Z.; Yang, C.; Wang, L.; Cowger, T.; Chen, H.; Todd, T.; Hekmatyar, K.; Zhao, Q.; Hou, Y.; Xie, J. Fe5C2 nanoparticles with high MRI contrast enhancement for tumor imaging. *Small* **2014**, *10* (7), 1245–1249.

(98) Cao, Z.; Feng, L.; Zhang, G.; Wang, J.; Shen, S.; Li, D.; Yang, X. Semiconducting polymer-based nanoparticles with strong absorbance

in NIR-II window for in vivo photothermal therapy and photoacoustic imaging. *Biomaterials* **2018**, *155*, 103–111.

(99) Liu, Z.; Liu, X.; Du, Y.; Ren, J.; Qu, X. Using Plasmonic Copper Sulfide Nanocrystals as Smart Light-Driven Sterilants. *ACS Nano* **2015**, *9* (10), 10335–10346.

(100) Song, J.-T.; Yang, X.; Zhang, X.-S.; Yan, D.-M.; Wang, Z.-Y.; Zhao, Y.-D. Facile Synthesis of Gold Nanospheres Modified by Positively Charged Mesoporous Silica, Loaded with Near-Infrared Fluorescent Dye, for in Vivo X-ray Computed Tomography and Fluorescence Dual Mode Imaging. *ACS Appl. Mater. Interfaces* **2015**, *7* (31), 17287.

(101) Ren, Z.; Chen, X.; Hong, L.; Zhao, X.; Cui, G.; Li, A.; Liu, Y.; Zhou, L.; Sun, R.; Shen, S.; Li, J.; Lou, J.; Zhou, H.; Wang, J.; Xu, G.; Yu, Z.; Song, Y.; Chen, X. Nanoparticle conjugation of Ginsenoside Rg3 Inhibits Hepatocellular Carcinoma Development and Metastasis. *Small* **2020**, *16* (2), 1905233.